



HAL
open science

A spatial statistical framework for the parametric study of fiber networks: application to fibronectin deposition by normal and activated fibroblasts

Anca-Ioana Grapa, Georgios Efthymiou, Ellen van Obberghen-Schilling, Laure Blanc-Féraud, Xavier Descombes

► To cite this version:

Anca-Ioana Grapa, Georgios Efthymiou, Ellen van Obberghen-Schilling, Laure Blanc-Féraud, Xavier Descombes. A spatial statistical framework for the parametric study of fiber networks: application to fibronectin deposition by normal and activated fibroblasts. *Biological Imaging*, In press, 10.1017/S2633903X23000247 . hal-04320315v1

HAL Id: hal-04320315

<https://hal.science/hal-04320315v1>

Submitted on 4 Dec 2023 (v1), last revised 8 Nov 2024 (v2)

HAL is a multi-disciplinary open access archive for the deposit and dissemination of scientific research documents, whether they are published or not. The documents may come from teaching and research institutions in France or abroad, or from public or private research centers.

L'archive ouverte pluridisciplinaire **HAL**, est destinée au dépôt et à la diffusion de documents scientifiques de niveau recherche, publiés ou non, émanant des établissements d'enseignement et de recherche français ou étrangers, des laboratoires publics ou privés.

This is an Open Access article, distributed under the terms of the Creative Commons Attribution-NonCommercial-NoDerivatives licence (<http://creativecommons.org/licenses/by-nc-nd/4.0/>), which permits non-commercial re-use, distribution, and reproduction in any medium, provided the original work is unaltered and is properly cited. The written permission of Cambridge University Press must be obtained for commercial re-use or in order to create a derivative work.

This peer-reviewed article has been accepted for publication but not yet copyedited or typeset, and so may be subject to change

during the production process. The article is considered published and may be cited using its DOI.

10.1017/S2633903X23000247

(0000), xx: 1–19

RESEARCH ARTICLE



CAMBRIDGE
UNIVERSITY PRESS

A spatial statistical framework for the parametric study of fiber networks: application to fibronectin deposition by normal and activated fibroblasts

Anca-Ioana Grapa¹, Georgios Efthymiou², Ellen Van Obberghen-Schilling², Laure Blanc-Féraud³ and Xavier Descombes¹*

¹Université Côte d'Azur, INRIA, CNRS, i3S, Nice, France

²Université Côte d'Azur, INSERM, CNRS, iBV, Nice, France

³Université Côte d'Azur, CNRS, INRIA, i3S, Nice, France

*Corresponding author. Email: xavier.descombes@inria.fr

Received xx xxx xxxx

Keywords: Fibronectin, Extracellular matrix, Oncofetal isoforms, Statistical parametric maps, Graph networks

Abstract

Due to the complex architectural diversity of biological networks, there is an increasing need to complement statistical analyses with a qualitative and local description of their spatial properties. One such network is the extracellular matrix (ECM), a biological scaffold for which changes in its spatial organization significantly impact tissue functions in health and disease. Quantifying variations in the fibrillar architecture of major ECM proteins should considerably advance our understanding of the link between tissue structure and function. Inspired from the analysis of functional magnetic resonance imaging (fMRI) images, we propose a novel statistical analysis approach embedded into a machine learning paradigm, to measure and detect local variations of meaningful ECM parameters. We show that parametric maps representing fiber length and pore directionality can be analyzed within the proposed framework to differentiate among various tissue states. The parametric maps are derived from graph-based representations that reflect the network architecture of fibronectin (FN) fibers in a normal, or disease-mimicking in vitro setting. Such tools can potentially lead to a better characterization of dynamic matrix networks within fibrotic tumor microenvironments and contribute to the development of better imaging modalities for monitoring their remodeling and normalization following therapeutic intervention.

Impact Statement

Quantification of phenotypic variation during tissue development and/or disease progression is essential for the understanding of different pathologies. All organs and tissues contain a non-cellular core component known as the ECM, composed of a network of macromolecules whose architecture depends on the pathophysiological state of the tissue. To derive a meaningful comparison of ECM between healthy and diseased tissues, computational frameworks that account for the localization of areas of phenotypic variation are needed. Here we introduce a novel framework for the statistical analysis of parametric maps calculated from graph-based representations of fibers composed of FN, a provisional ECM component that guides ECM organization. Our framework is inspired from the statistical analysis of fMRI parametric maps and is embedded in a machine-learning model to compare distinct states of ECM fiber networks, both quantitatively and qualitatively. These methods may be further developed and implemented in ECM profiling of tumor/fibrotic tissue to provide both valuable insight into specific roles of ECM landscapes and their remodeling in disease, and more specific diagnostic, prognostic, and predictive companion biomarkers in the clinic.

1. Introduction

During normal development and disease progression, tissues undergo various remodeling processes, which can, in turn, affect their physical characteristics, yielding heterogeneous morphologies. Automated detection and quantification of these phenotypic changes in the tissue landscape are essential for an accurate characterization of a given pathology. Statistical tests that are commonly used for the comparison of two different conditions based on the distributions of morphological properties, are applied at a global scale, and do not account for any explicit spatial information. Here we were interested in exploiting a known spatial statistical approach (historically proposed for functional imaging (fMRI) analysis) and recasting it into a machine learning framework to facilitate the comparison of two tissue conditions. Within the proposed framework relying on statistical parametric mapping (SPM)^(1,2), the comparison of various physical tissue characteristics is thus achieved both at a quantitative and qualitative level. It does so by enabling the localization and quantification of local variations of certain morphological properties in the sample that are significantly different and relevant to a given pathology.

SPM is a long-established methodology, specifically developed in fMRI for the detection of significantly activated regions of the brain in a given image sample. Mapping of activated regions is achieved by assessing the probability of random occurrences of activated regions with pixel intensities higher than a given threshold or having a larger spatial extent at lower intensities.

To address the need for taking spatial localization into account when designing frameworks that can discriminate between two different conditions of a given tissue, we recast the SPM paradigm into a data-driven machine learning framework for detection of significant parametric differences between the two classes. Thus, we train the model on a given population (for example the control case) and we detect local areas in the second population of samples that deviate from this model. In our work, we applied this approach to the characterization of two distinct states of the extracellular matrix (ECM), a non-cellular component of organs and tissues.

The ECM is a biological scaffold with multiple forms and functions. It acts as a biomechanical and structural support ensuring tissue integrity, it relays chemical and physical signals to the residing cells through cell surface receptors and it sequesters growth factors and regulates their bioavailability. The composition and architecture of the ECM is tissue- and organ-specific, and depends on the pathophysiological state of the tissue (i.e. normal vs diseased)⁽³⁾. For example, while a healthy connective tissue displays a loose meshwork-like ECM, a fibrotic or cancerous stroma is characterized by the presence of dense, aligned ECM fibrils. Thus, the physical and structural traits of the tumor matrix have recently drawn much attention as cancer hallmarks and potential therapeutic targets^(4,5). Collagen, the most abundant matrix component, has been extensively investigated in this context and several studies addressing its structural features and their association to cancer progression, metastasis and treatment have been published^(6–8). Collagen deposition, however, depends on the presence of fibronectin (FN), a dimeric glycoprotein that forms a provisional matrix framework to which other ECM components integrate to generate a mature ECM^(9,10).

During inflammation, wound healing, or tumor development, the expression of FN is induced and assembled into an insoluble matrix. This FN produced primarily by fibroblasts, corresponds to cellular FN, as opposed to plasma FN. At the molecular level, cellular FN differs from plasma FN by the presence of one or two 90-amino acid-long alternatively spliced sequences, termed Extra Domains (EDB and EDA). Extra Domain-containing FN displays enhanced assembly, making it the most prevalent FN isoform in diseased tissue. This enhanced FN deposition results in a highly modified ECM architecture with increased fiber density, directionality and stiffness, that together tune cellular responses and impact tissue homeostasis⁽¹¹⁾.

Despite the pivotal role of FN in health and disease⁽¹²⁾, comprehensive studies of FN fiber features are lacking. In our previous work⁽¹¹⁾, we set out to develop a robust pipeline of numerical analyses for

the extraction of biologically relevant metrics to discriminate among different isoforms of cellular FN from confocal microscopy images of FN matrices. The goal of the present work was to capture and analyze physiologically relevant ECM fibrillar features that discriminate between normal and diseased states. To that end, we generated FN-rich ECM using an *in vitro* model of cell derived matrices (CDMs) produced by normal fibroblasts, or fibroblasts activated with transforming growth factor beta 1 (TGF- β 1), a fibrosis-promoting cytokine known to induce a tumor-like state.

Herein we show that the proposed SPM-based machine learning methodology can be used to distinguish between normal and disease-mimicking FN fiber networks. To capture and localize significant differences of fiber properties, we built parametric maps, such as fiber length and pore directionality relying on a graph-based fiber representation that recapitulates the FN fiber networks from confocal microscopy images. In the following sections, we will provide an outline of the proposed methodology applied to SPMs and describe how our proposed machine-learning embedding can yield significant localized parametric variations between different tissue states.

2. Statistical parametric maps (SPM) and Gaussian Random Fields

2.1. SPM statistical framework

Statistical parametric maps are used to evaluate the probability of change in every pixel by using decision tests based on the magnitude of the SPM values (i.e. the peak intensity of a cluster in SPM) as well as the spatial extent of these clusters formed at certain intensity thresholds⁽¹⁾. The value of the pixel intensity reflects a parametric value of interest. Hence these (2D) maps are constructed to reflect the spatial variation of a measured parameter which is important for discriminating between two given classes with regards to its intensity and area. In this way, clusters of high intensity of a SPM can correspond to a high localized parametric variation, while a large region reflects a spatially extended area of variation.

Our proposed spatial statistical learning framework relies on graph-derived parametric maps to quantify and simultaneously localize statistically significant differences across normal and disease-mimicking FN organization. Using the pixel intensity of the maps along with the extent of the region area, these differences can be assessed both quantitatively and qualitatively, and detected as anomalies with respect to a Gaussian Random Field (GRF), corresponding to regions within the maps that cannot be explained by the GRF model learnt from the reference population. Hereafter, we describe the theoretical framework of GRF⁽¹³⁾ that enables the statistical analysis of tissue parametric maps.

GRF, whose marginal distributions are Gaussian vectors $X = (X_{(1)}, \dots, X_{(n)})$, are characterized by the probability density function:

$$f_X(x) = (2\pi)^{-n/2} |V|^{-1/2} \exp\left[-\frac{1}{2}(x - \mu)V^{-1}(x - \mu)^T\right] \quad (1)$$

where $\mu = (E(X_{(i)}))_{i \in \{1, \dots, n\}}$ is the expectation and $V = (E[(X_{(i)} - \mu_{(i)})(X_{(j)} - \mu_{(j)})])_{i \in \{1, \dots, n\}, j \in \{1, \dots, n\}}$ is the covariance matrix.

We consider clusters of pixels as connected components that are formed based on 8-pixel connectivity. Hence, upon image binarization according to a chosen threshold, the pixels (with intensity equal to 1) are grouped together in disjoint components (including single pixel components) based on similar values of the neighbouring 8 pixels. It was shown in⁽¹³⁾, and later adopted in fMRI-specific studies^(1,2,14), that for large thresholds t , the clusters are independent and the expectation of the number of clusters at a threshold t , of an image modeled by a zero-mean, homogeneous Gaussian field of dimension 2, is estimated by the expected Euler characteristic of the excursion set of the GRF:

$$E[m_t] = S(2\pi)^{-3/2} |\Lambda|^{1/2} t \sigma^{-3} \exp - \frac{t^2}{2\sigma^2} \quad (2)$$

90 where:

- 91 • m_t represents the number of clusters at a certain threshold t
- 92 • S is the number of pixels of the image
- 93 • Λ is the covariance matrix of partial derivatives of the GRF
- 94 • σ is the standard deviation of the GRF

95 Similarly, the mean value of the number of clusters at a threshold $t + H_0$ can be written as such:

$$E[m_{t+H_0}] = S(2\pi)^{-3/2} |\Lambda|^{1/2} (t + H_0) \sigma^{-3} \exp - \frac{(t + H_0)^2}{2\sigma^2} \quad (3)$$

96 Considering $x_0 = t + H_0$ as the intensity peak of a cluster (at threshold t), one can estimate the probability
 97 that a cluster (at a threshold t , having an intensity peak higher or equal to x_0 , denoted $C_t^{H_0}$) belongs to a
 98 realization of this GRF, G_r . This probability, as shown in ⁽¹⁾, termed P_H , can be seen as the likelihood
 99 of a cluster (formed at threshold t) of having an intensity peak higher or equal to $t + H_0$ ⁽¹⁾:

$$P(C_t^{H_0} \in G_r) = \frac{E[m_{t+H_0}]}{E[m_t]} = \frac{x_0}{t} \exp \frac{t^2 - x_0^2}{2\sigma^2} \quad (4)$$

100 Next, we were interested in the estimation of the probability that a cluster (at a threshold t) belongs to a
 101 realization of GRF, depending on its surface (spatial extent - number of pixels). To estimate the number
 102 of pixels (n_t) of a cluster at a threshold t , we use the following equation from ⁽²⁾:

$$E[n_t] = \frac{E[N_t]}{E[m_t]} \quad (5)$$

103 where N_t is the number of pixels at of higher intensity than t , and m_t is the number of clusters at the
 104 threshold t . Since the intensity values follow a normal (zero mean value) distribution, the expectation
 105 of N_t is the following ⁽²⁾:

$$E[N_t] = S \int_t^\infty (2\pi\sigma^2)^{-1/2} \exp - \frac{x^2}{2\sigma^2} dx = S\Phi_\sigma(-t) \quad (6)$$

106 where $\Phi_\sigma(-t)$ is the complementary cumulative distribution function. It follows, then, based on
 107 equations (2,5,6) that one can approximate the mean value of n_t , accordingly:

$$E[n_t] = \frac{E[N_t]}{E[m_t]} = \frac{\Phi_\sigma(-t)}{(2\pi)^{-3/2} |\Lambda|^{1/2} t \sigma^{-3} \exp - \frac{t^2}{2\sigma^2}} \quad (7)$$

108 Furthermore, n_t follows an exponential distribution law ⁽¹⁵⁾, which is commonly defined by a parameter
 109 λ_t , (the inverse of the mean expected value of the random variable). Consequently:

$$P(n_t = x) = \lambda_t \exp(-\lambda_t x) \quad (8)$$

110 where $\lambda_t = \frac{(2\pi)^{-3/2} |\Lambda|^{1/2} t \sigma^{-3} \exp - \frac{t^2}{2\sigma^2}}{\Phi_\sigma(-t)}$

111 It follows then that the approximation for the probability P_S of a given cluster $C_t^{S_0}$ having a spatial
 112 extent S greater than S_0 , is given by the following formulation, as shown in ⁽²⁾:

$$P(C_t^{S_0} \in G_r) = P(n_t \geq S_0) = \exp(-\lambda_t S_0) = \exp\left(\frac{(2\pi)^{-3/2} |\Lambda|^{1/2} S_0 t \sigma^{-3} \exp\left(-\frac{t^2}{2\sigma^2}\right)}{\Phi_\sigma(-t)}\right) \quad (9)$$

113 In the following section, we illustrate our proposed approach using a simple scenario of a simulated
 114 GRF, in which the model parameters are estimated from a 'normal' sample, to detect significant changes
 115 in an 'abnormal' example.

116 2.2. Test for anomaly detection using synthetic data

117 To better understand the concept of detecting statistical abnormalities in a GRF realization, we con-
 118 sidered a simple scenario which includes a synthetic example (normal), representing a simulation of a
 119 GRF of zero mean (Figure 1A). To this example we added 6 foreign objects representing ellipses with
 120 different surfaces, and intensity levels. The aim was to use our approach to detect these 6 objects within
 121 the abnormal sample, showcasing the potential to localize these anomalies at various thresholds, based
 122 on the maximum intensity of the different regions detected at each threshold, or their spatial extent
 123 (Figure 1B). The null hypothesis is that clusters of pixels computed at different thresholds in the abnor-
 124 mal example belong to a realization of the same GRF as the normal sample. The hypothesis is rejected
 125 if either P_H or P_S is less or equal than a p-value (pval) of 0.05.

126 Our method learns the GRF model parameters from the reference example, and then uses these
 127 parameters to compute the two probabilities of belonging to GRF for each region at various thresholds
 128 in the abnormal example. As shown in Figure 1A and Figure 1B, the current method, compared to a
 129 naïve hard thresholding (threshold equal to 10), is better suited to localize the abnormal elements, i.e.
 130 ellipses, at thresholds equal to (10,15,20). One could opt to jointly consider intensity and surface-based
 131 criteria when selecting the detected objects, which in this scenario, would lead to selecting the 6 ellipses
 132 together with one false positive (Figure 1C). It is noteworthy that the same false positive is detected on
 133 the reference image, which is consistent with the definition of the pval.

134 2.3. Machine-learning embedded in a GRF-based statistical parametric map framework

135 Providing both a quantitative and a qualitative assessment of the parameter variations is imperative for
 136 the study of spatial heterogeneity of fibers in pathological conditions. We were interested in leverag-
 137 ing our proposed framework for the comparison of two distinct conditions, normal and pathological
 138 ECM, given parametric maps that reflect various fiber characteristics. To do so, we learnt the GRF
 139 model's parameters from the normal samples and using these parameters, we subsequently determined
 140 the probabilities of regions within the pathological conditions belonging to the same GRF, casting the
 141 original framework into a machine-learning setting. More specifically, we applied our proposed frame-
 142 work to determine whether fiber length and pore directionality can discriminate between normal and
 143 disease-mimicking states. While topographical differences between ECM of healthy and tumor tissue
 144 have been described⁽⁶⁾, mainly for collagen, no current computational study can, to our knowledge,
 145 simultaneously localize and quantify them.

146 First, we describe the principle behind the proposed approach (Figure 2), which relies on model-
 147 ing the normal maps as realizations of a GRF and testing this hypothesis on tumor-like maps⁽²⁾. We
 148 hypothesized that the tumor-like maps are realizations of the GRF learnt from the reference maps and
 149 determined a set of probabilities that characterize a degree of belonging to the GRF, for certain con-
 150 tiguous regions (clusters) at various intensity thresholds. In other words, the current statistical analysis
 151 identifies those foreign regions with respect to the reference GRF, within both types of maps, under the
 152 null hypothesis (i.e., at a given pval).

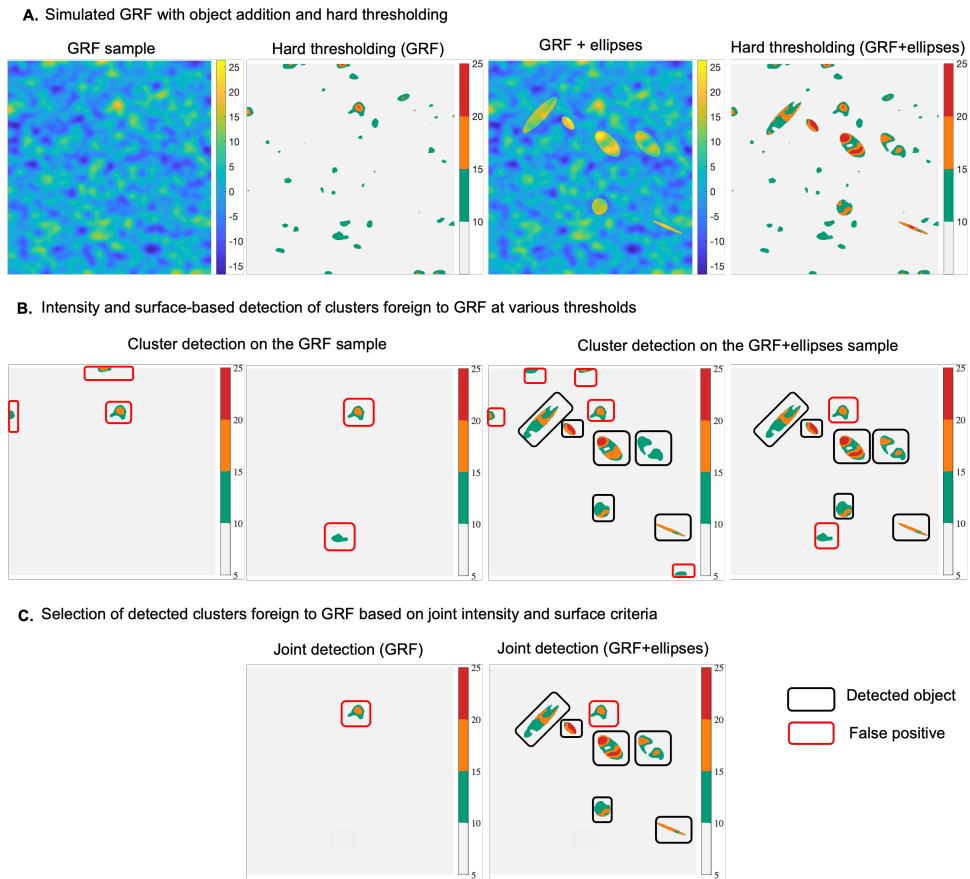


Figure 1. (A) Realization of a GRF of zero-mean (normal case) and addition of 6 different sized ellipses (abnormal case), along with intensity-based hard thresholding for each case respectively (at a threshold $t = 10$ pixels) (B). Intensity and surface-based detection at $pval \leq 0.05$, and at thresholds equal to (10,15,20, see colorbar). GRF sample detection will typically contain false-positive detections while within the abnormal case (GRF+ellipses), all 'foreign' objects, i.e ellipses are detected at $pval \leq 0.05$, along with a few false-positives. (C). Clusters that are jointly detected based on the surface and intensity criteria are selected for both normal and abnormal samples .

153 In this context, the parametric maps are described by the union of two classes of pixels: those rep-
 154 resenting a realization of a GRF modeling the normal case, and those that are foreign to the GRF. We
 155 expect these foreign elements to occur in regions with very high pixel intensity and/or in larger clusters
 156 taken at a specific threshold.

157 Modeling the parametric maps with GRF is only possible upon gaussianization (i.e. conversion of
 158 the empirical distributions into normal distributions) of the GRF marginal distributions. In practice, we
 159 only performed the gaussianization of the first-order marginal distribution of the GRF, i.e. the image
 160 intensity histogram, considering that the parameter maps under study were smooth enough. Therefore,
 161 the image intensity histogram was the only distribution to be gaussianized using an approach based on
 162 optimal transport^(16,17) (Supplementary Figure S1). Thereby, the resulting intensity histogram follows
 163 a normal distribution of zero mean with identical variance as the empirical native histogram.

164 To estimate the likelihood of a certain cluster formed at an intensity threshold t to belong to a GRF,
 165 depending on the maximal intensity of this cluster, we relied on the formulations taken from the theory

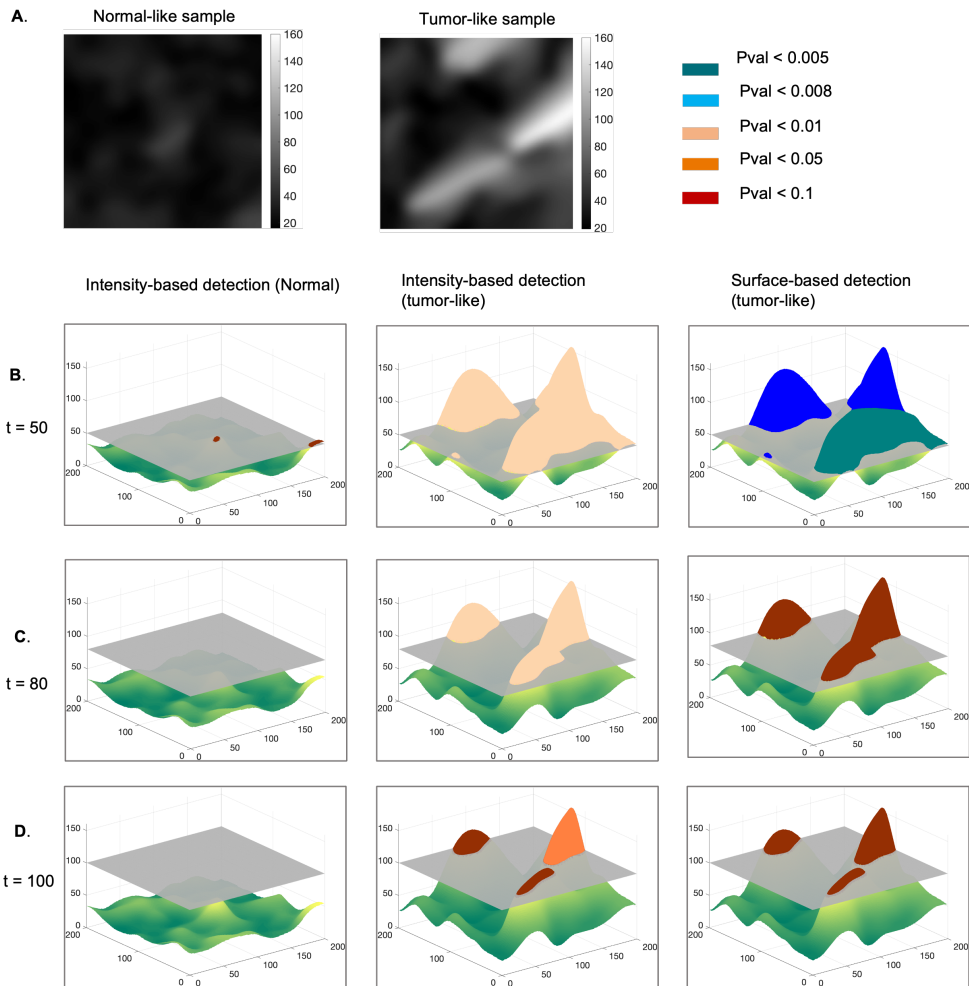


Figure 2. Methodology for statistical detection of foreign regions to a GRF, in an example of a sample representing normal and tumor-like parametric maps. (A) Normal and tumor-like fiber length maps. The normal sample is modeled as a realization of a GRF, and we assume that the tumor-like sample is a realization of the same process. Clusters of regions with an intensity higher than a given threshold, $t = 50$ (B), $t = 80$ (C), $t = 100$ (D) are found to be statistically different to the GRF, with respect to a p val, depending on the cluster maximum intensity value or their surface .

of random fields⁽¹³⁾, as previously described. Considering $x_0 = t + H_0$ as the intensity peak of a cluster (at intensity threshold t), one can estimate the probability that a cluster having an intensity peak higher or equal to x_0 , belongs to a realization of GRF. This probability can be seen as the likelihood of a cluster (taken at threshold t) of having an intensity peak higher or equal to $t + H_0$ (Equation 4). Furthermore, as previously shown, the approximation for the probability of a given cluster having a spatial extent S greater than S_0 is given by Equation 9. At $pval \leq 0.05$, the clusters of pixels identified at t are considered significantly different from the normal GRF model.

In our experiments, we focused on two different FN parametric maps that could potentially discriminate between normal and pathological conditions, fiber length and pore directionality maps, in both reference and disease-mimicking states. We embedded the SPM framework, initially developed to analyze single datasets independently, into a machine learning paradigm. To evaluate the differences

177 between two given groups of maps (e.g., FN in normal state vs disease-like state), we considered one
 178 of the groups as the normal realization of the GRF which we divided into a learning set and a smaller
 179 test set. The second group was tested for anomalous regions, therefore all the images belonging to this
 180 group were considered part of the test set. The proposed method learns the normal GRF model spe-
 181 cific parameters, i.e. the average value of λ_j, σ_j , from the training set. These learnt parameters during
 182 the learning phase were subsequently used to compute the two relevant probabilities, P_H and P_S , as
 183 described hereafter:

184 For all the images I_j (previously Gaussianized) in the learning set:

- 185 • Computation of Λ_j (Equation 2, empirical estimator of the covariance of partial derivatives of
 186 I_j). If for an image function $f \in \mathbb{R}^2$, we consider its gradient vector $\nabla f = (f_x, f_y) = (\frac{\partial f}{\partial x}, \frac{\partial f}{\partial y})$,
 187 then $\Lambda_j = \text{cov}[f_x, f_y] = E[(f_x - E[f_x])(f_y - E[f_y])]$.
- 188 • Computation of σ_j , as the I_j 's sample standard deviation.

189 The last step involves storing the average Λ_m, σ_m of the learning dataset.

190 During the test phase, for all the clusters identified at a threshold t within the test set, P_H and P_S
 191 are evaluated using the model's previously learnt parameters. At $pval \leq 0.05$, the clusters are sig-
 192 nificantly different from the normal GRF model, and can be considered for subsequent analysis (e.g.
 193 quantification).

194 For all the images I_j in the test set:

- 195 • Gaussianization of each sample image I_j . The result is a new image I_g , whose histogram is
 196 Gaussian with identical variance to that of I_j .
- 197 • For a given list of thresholds $T = (t_1, t_2, \dots, t_n)$:
 - 198 – Binarization of the image I_g according to the threshold t_i
 - 199 – Once the list of connected components in the binary image resulted from thresholding is
 200 achieved, then for every (labeled) connected-component (l_1, l_2, \dots, l_p) :
 - 201 * Evaluation of P_H using the learnt model parameter σ_m .
 - 202 * Evaluation of P_S using the learnt model parameters Λ_m, σ_m .

203 3. Generation of FN variant-specific fibroblast-derived matrices and induction of a tumor-like 204 state

205 To test our method, we utilized a previously established in vitro system to generate normal and disease-
 206 mimicking ECMs by normal mouse fibroblasts. Fibroblasts are the major ECM-producing cells of
 207 tissues. In pathological conditions (e.g. tumors), quiescent fibroblasts become activated by environ-
 208 mental cues that induce their phenotypic conversion to 'myofibroblasts' with a pro-tumoral phenotype
 209 (Figure 3A, top). This process is characterized by the upregulation of cellular FN expression, actin
 210 reorganization and increased cell contractility that result in their elongation and the deposition of a
 211 highly anisotropic FN-rich ECM⁽¹¹⁾. In vitro, these changes can be mimicked by treating normal resting
 212 fibroblasts with TGF- β 1, a potent cytokine involved in fibroblast activation in the tumor microenvi-
 213 ronment⁽¹¹⁾. For our analyses, FN-rich normal or tumor-like matrices were generated by presenting
 214 FN-null mouse embryo fibroblasts with recombinant cFN (prepared as previously described⁽¹¹⁾), as
 215 schematized in Figure 3B. For the induction of a tumor-like phenotype, fibroblasts were incubated with
 216 TGF- β 1 (Figure 3C). Cultures were decellularized after 7 days, and the resulting cell-derived matrices

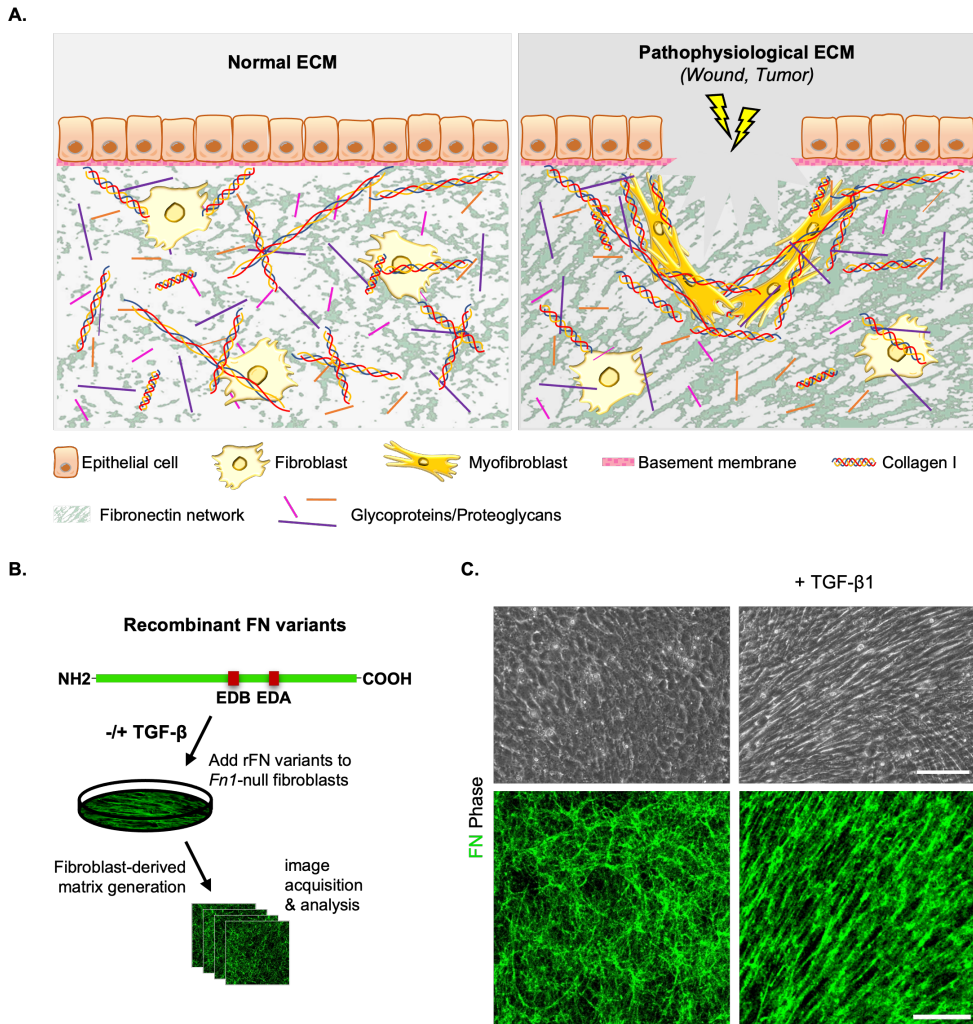


Figure 3. (A) Schematic representation of a simple cuboidal epithelium displaying the different architectures of the underlining ECM in normal (left) and pathological conditions (right). (B) Workflow diagram featuring the linear structure of the purified recombinant FN (rFN) variants and the relative positions of the alternatively spliced Extra Domains, the generation of fibroblast-derived matrices, and image acquisition and analysis. (C) Phase contrast images (top row) of FN-null mouse fibroblasts presented with FN B+A+ variant (15 $\mu\text{g}/\text{ml}$) in the presence or absence of TGF- β 1 (5 ng/ml) to mimic the changes that take place in the tumor/fibrotic microenvironment. After removal of the cells, matrices were stained with a rabbit-anti-FN polyclonal antibody and visualized with confocal microscopy. Scale bars: phase, 100 μm ; IF, 50 μm .

217 were visualized by immunofluorescence staining and confocal microscopy. Organization of variant-
 218 specific FN matrices in normal and activated states was then quantitatively analyzed, as described
 219 below.

4. Generation of parametric maps from confocal images of ECM

4.1. Fiber detection using Gabor filters and graph extraction

To detect and quantify fiber-specific properties of FN networks (Figure 4A), we developed a pipeline that was primarily utilized for the extraction of local topological fiber properties from 2D confocal microscopy images, as described previously⁽¹¹⁾. Existing ECM analysis methods focusing on collagen exploit alternative fiber detection techniques, such as Fast Fourier Transform bandpass filters⁽¹⁸⁾, ridge detection⁽¹⁹⁾, or fast discrete curvelet transform⁽²⁰⁾, which is arguably the best suited method to detect curvilinear anisotropic objects, among the previous options. The latter option was used in conjunction with a fiber extraction algorithm. Our method relies on a more flexible detection scheme using Gabor filters, thereby avoiding translation/rotation errors, and unlike other methods, associates graph networks to fiber morphological skeletons, enabling diverse fiber analyses. The current study builds on our previously described fiber enhancement approach⁽¹¹⁾, for which the key steps are summarized as follows. Fibers in confocal images (Figure 4A) were detected and enhanced using Gabor filters (Supplementary S1) tailored to capture a range of different fiber elements that occur at multiple frequencies and orientations (Figure 4B). Subsequently, we opted for a graph-based framework to construct morphological fiber skeletons (Figure 4C) that would ultimately provide a geometrical characterization of fiber patterns. Further steps for improving fiber representation (e.g. fiber pruning, post-processing fiber reconnection) were implemented as described in previous work⁽²¹⁾. Graphs (i.e. collections of nodes connected by edges) are powerful tools for the structural and pattern analysis of objects, which can be utilized for the mathematical study of relations between entities, including fiber-like object detection^(22,23).

Within our current analysis, we employ two different graph types to measure fiber-specific properties. First, graphs are used to depict a morphological skeleton representation (Figure 4D - left). Here, the nodes represent either fiber crosslinks (actual fiber junctions or junctions due to the 2D projection of the network onto the image plane) or fiber ends, and the edges capture the fiber length between two given nodes. We previously showed how such a representation can provide a description of distinct local features among four FN variant networks, in a normal state⁽¹¹⁾.

The second type of graph-based representation introduced in this work (Figure 4D - right) is meant to simplify fiber delineation, as described hereafter. Starting from the skeleton graph, we kept all nodes corresponding to fiber extremities, and connected all pairs of nodes with a straight line, if a fiber had previously been identified. For the sake of simplicity, we refer to fiber length as the length of any straight line connecting a pair of graph nodes.

We note that both representations are useful to extract different local or global fiber properties. The graph-based skeleton fiber delineation faithfully represents (according to a visual assessment performed by a trained biologist) the geometrical and topological properties of the fibers from the 2D confocal images, while the Gabor-specific (e.g. fiber local orientation, thickness) and graph-derived parameters (e.g. fiber length, number of nodes, etc.) are linked to meaningful physical fiber attributes. This biologically relevant representation enabled us to develop here a statistical analysis of the variation of certain fiber parameters for both the normal and a tumor-like state of the FN networks.

4.2. Generation of fiber parametric maps from graph-derived fiber representations

We next sought to develop a statistical framework for differentiating between parametric maps of activated and non-activated FN network configurations, computed from graph-based fiber representations. To create tissue variation maps (Figure 5), we considered different fiber attributes computed from graphs, representing either morphological skeletons (Figure 5A) or simplified graph depictions (Figure 5C). This framework is exemplified on two different types of parametric maps (Figure 5B,D) reflecting discriminative features, namely the individual fiber lengths (i.e. the length of the connecting line between two graph nodes), and the fiber pore ('gap') directionality (i.e. the inverse value of the absolute difference between the median and individual pore orientation).

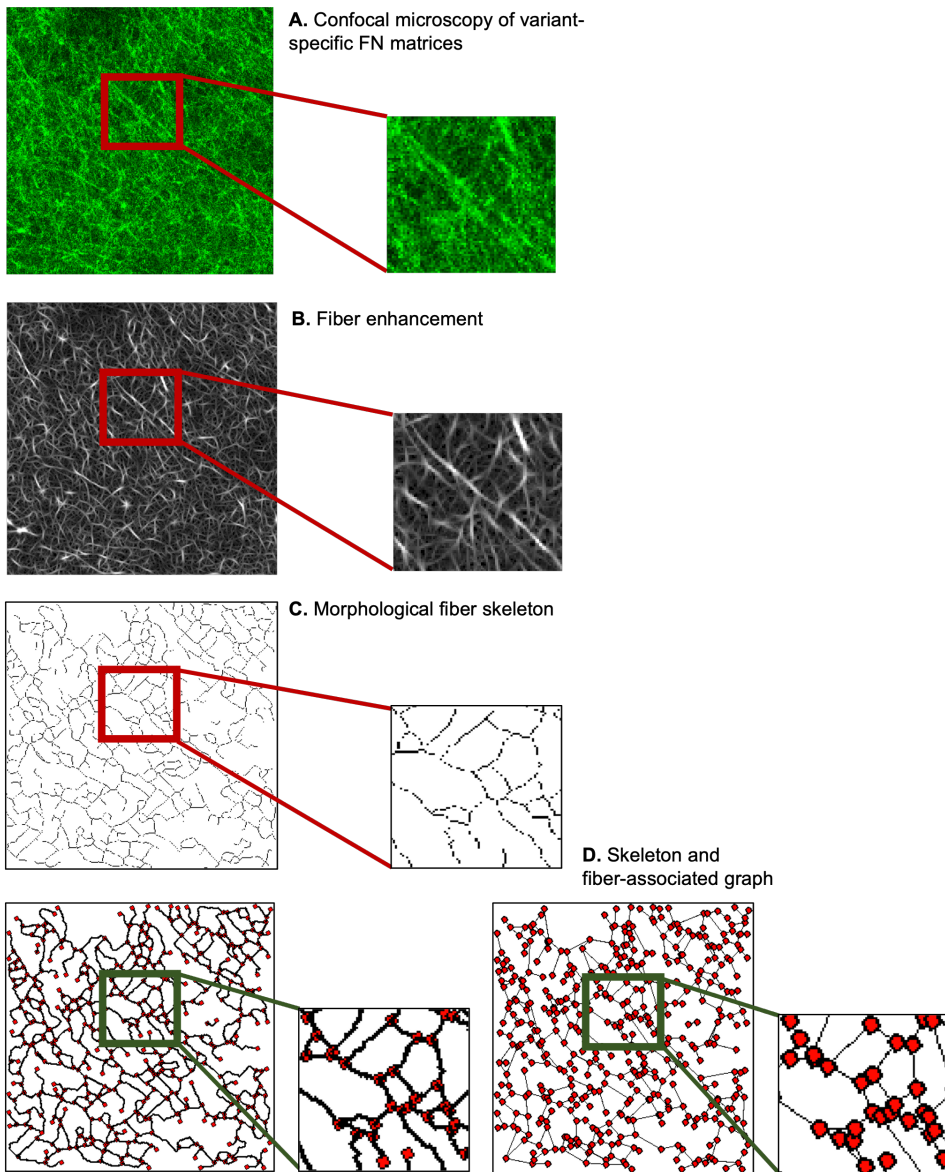


Figure 4. Fiber enhancement and graph-based representation starting from confocal 2D images. (A) Representative region (512x512 pixels) of a sample image (FN B-A+) at a resolution of $0.27 \mu\text{m}/\text{pixel}$. (B) Fiber enhancement with Gabor filters (C) Morphological fiber skeleton extraction (D) Skeleton-based graph (left) and simplified graph representation (right) which is derived from the latter .

268 To build a fiber length map (Figure 5D), the starting point was the simplified graph-based representa-
 269 tion, where nodes depict fiber ends or crosslinks, and fibers are represented by the straight connecting
 270 line between these nodes. During the next step, we identified the 2D pixels coordinates that approximate
 271 the straight line between the nodes⁽²⁴⁾ and assigned the length value of the connecting line to each one
 272 of the corresponding pixels. The last step for generating dense fiber length maps consists of including
 273 the extrapolation of the fiber length values⁽²⁵⁾ and smoothing of this result with a Gaussian kernel. Con-
 274 cerning the pore directionality parametric maps (Figure 5B), the starting point was the skeleton graph.

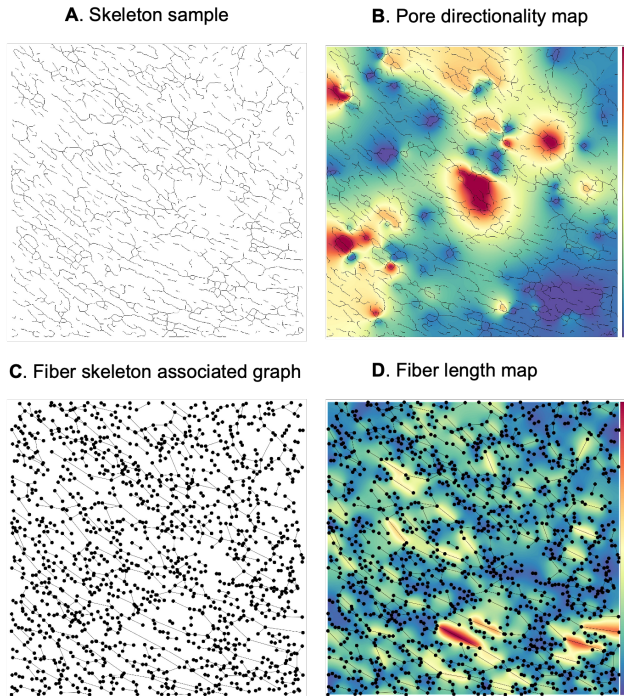


Figure 5. Computation of fiber parametric maps: (A) Starting from the skeleton graph (FN B-A+ disease-like sample, 1024x1024 pixels, 0.27 $\mu\text{m}/\text{pixel}$), a pore directionality map is derived (B), as the inverse value of the difference between the median pore angle and each individual one. (C) Starting from the fiber skeleton associated graph, a parametric map (fiber length, (D)) associates the fiber length, in pixels, to each corresponding connecting line .

275 Pore orientation was computed by first fitting ellipses to each pore and was subsequently obtained by
 276 measuring the angle i between the horizontal axis and the major ellipse axis. Pore median value was
 277 then subtracted from each i to remove image rotations from the analysis. Finally, the inverse absolute
 278 value of the resulting individual score per pore (indicative of the directionality) was assigned to all pix-
 279 els filling its corresponding surface, and subsequently smoothed out with a Gaussian kernel. High values
 280 within the pore directionality maps correspond to those regions in which pores are oriented similarly to
 281 the median pore angle, ultimately indicating regions characterized by a predominant pore orientation.

282 To complement these analyses, we developed a graphical user interface (GUI) for the analysis of a
 283 single image/batch displaying fiber networks. Fibers are enhanced using Gabor filters and represented
 284 by graphs. Parametric maps, such as fiber length and pore directionality maps can subsequently be
 285 derived. The output results can be written into .png image files, while the fiber specific graph/Gabor-
 286 derived features are collected in .csv files. The MATLAB source code and sample images for testing
 287 can be found on the GitHub platform, at github.com/aigrapa/ECM-fiber-graph.

288 4.3. Test for anomaly detection using fiber network simulations

289 To simulate fiber networks, we considered a set of scattered point patterns P_d , where P_d is the set
 290 of points $(x + n_x * d, y + n_y * d)$, for n_y odd, and $(x + n_x * d, y + (n_y + 0.5) * d)$ for n_y even,
 291 $n_x, n_y, d \in \mathbb{N}$. Random noise was added at the points' location : $\forall p = (X, Y) \in P_d, p' = (X + \eta_x, Y + \eta_y)$,
 292 where η_x and η_y follow a uniform law between 0 and N , $N \in \mathbb{N}$. In this way, we generated two
 293 patterns P_1 and P_2 using different values for d , as well as a mask M (for the second scenario),

294 which is an image equal to zero except for specific areas (e.g. ellipses Figure 6A). We consider P as:
 295 $\{(x, y) \in P_1 : M(x, y) = 0\} \cup \{(x, y) \in P_2 : M(x, y) \neq 0\}$. The fibers were subsequently defined by
 296 the edges of the Delaunay graph of P .

297 The first isotropic fiber network corresponds to a 'normal' example ($d = 30, N = 20$), while the fiber
 298 network with local defects (i.e. fibers are more elongated in the regions containing 'defects', corre-
 299 sponding to the three regions within the mask) is considered here an 'abnormal' example ($d \in \{40, 50\}$,
 300 $N = 20$) (Figure 6A). Fibers were detected as explained in 4.1, and fiber graphs were correspondingly
 301 derived for both images (Figure 6B). Starting from the graph-based fiber representation, fiber length
 302 parametric maps were generated accordingly, as described in 4.2 (Figure 6B), and subsequently 'gaus-
 303 sianised', as explained in 2.3. We were interested in applying the same principle described in 2.2, in
 304 order to detect the three regions of fiber length variation corresponding to the proposed ground-truth
 305 mask (Figure 6A). According to this principle, the null hypothesis is that clusters of pixels in the para-
 306 metric map, computed at different thresholds in the abnormal example, belong to a realization of the
 307 same GRF as the normal sample. The method learns the GRF model parameters from the parametric
 308 map corresponding to the reference-normal example, and then uses these parameters to compute the
 309 two probabilities of belonging to GRF, for each region at various thresholds, in the abnormal sample's
 310 parametric map, using an intensity or surface-based criterion. Different regions were identified at var-
 311 ious thresholds, for both intensity and surface-based detection (Figure 6C), at a $p\text{-val} \leq 0.05$. By only
 312 keeping the regions which were detected at a certain threshold (surface-based detection) having a non-
 313 null intersection with the clusters detected according to the intensity-based criterion, we were able to
 314 accurately detect the three regions of fiber length variation, as well as two additional false positive
 315 smaller regions within the parametric map of the fiber network with local defects.

316 5. Results - statistical analysis of fiber parametric maps

317 The graph-based representation of FN networks enabled the subsequent design of a novel framework
 318 to perform a spatial statistical analysis of ECM patterns, using graph-derived statistical parametric
 319 maps. This methodology was applied for a quantitative and qualitative analysis of fiber length and pore
 320 directionality differences, across all FN variant networks in normal and tumor-like states. We were
 321 thus interested in determining whether the proposed SPM analysis of the selected spatial fiber features
 322 could reveal significant variant-specific differences between the FN variant networks in normal (N) and
 323 tumor-like (T) states.

324 To apply our framework to the available data, we first divided the available sets of confocal images
 325 (1024×1024 pixels, $0.27 \mu\text{m}/\text{pixel}$; 70 images/variant for normal FN (N) and 65 images/variant for
 326 tumor-mimicking FN networks) as follows. For comparison of (N) vs (T) FN networks, we considered
 327 50 (N) samples as the learning dataset, 20 (N) as a test set for normal, and 65 (T) as a test set for
 328 disease-like networks. In all scenarios, a cluster is considered significantly different from the normal
 329 GRF model at $p\text{-val} \leq 0.05$. Anomalies in fiber length (Figure 7A) detected using either intensity or
 330 surface-based criteria (Figure 7B,C) and pore directionality maps (Figure 8A, B,C) were detected at a
 331 few intensity thresholds (e.g. 70,80,90) and (10,12,14), respectively (Figure 7, Figure 8). Thus, using
 332 our approach, differences in fiber length and pore directionality could be localized in regions formed
 333 at different intensity thresholds. This property is very useful for obtaining a qualitative analysis of
 334 parametric maps, where clusters of pixels that are statistically different from a normal model can be
 335 localized.

336 For the quantitative analysis of tissue parametric variations, we set out to determine significant dif-
 337 ferences between FN variant networks through the average number of identified foreign clusters, as
 338 well as the average cluster area per image. It is noteworthy that the group for which anomalous clusters
 339 were found at superior thresholds, had higher parametric values than in the normal model. For example,
 340 if significantly different regions occur in the tumor-mimicking matrices compared to the normal ones,

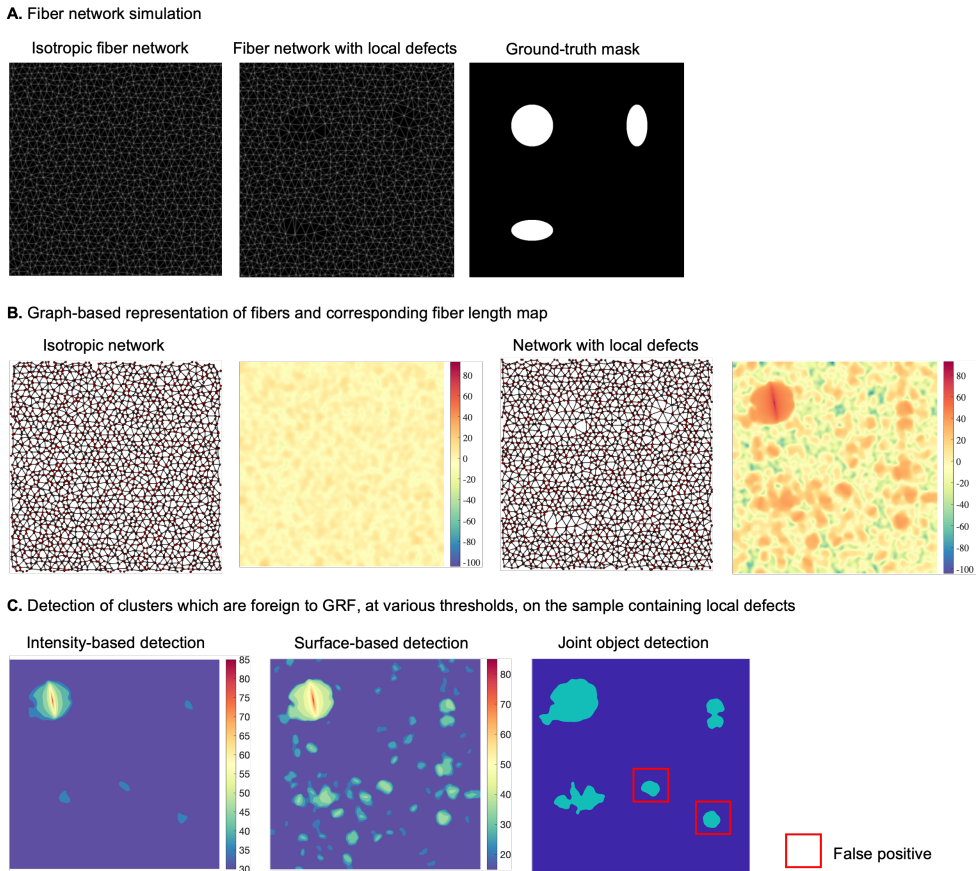


Figure 6. Anomaly detection within parametric maps of simulated fiber networks (A) Simulations of fiber networks (1024x1024 pixels), isotropic (left) and with local defects (center), ground-truth mask (right). (B) Graph-based representations of fiber networks, and corresponding fiber length parametric maps for both samples. (C) Detection of anomalous clusters with respect to the normal GRF model (at $p_{val} \leq 0.05$), at various thresholds, on the parametric map containing defects, for intensity-based (left) and surface-based criteria (center). The regions detected at a threshold of 20, based on a surface-based criterion having a non-null intersection with those detected at a threshold of 35, according to an intensity-based criterion (right).

341 with respect to fiber length, then fibers are statistically more elongated within former networks than
 342 normal counterparts. As shown in Figure 7,8, we found both fiber length and pore directionality to be
 343 significantly different for pairwise comparisons of normal and tumor-like FN variant networks. Essen-
 344 tially, the latter type of FN architecture relative to normal ECM, is represented by statistically longer
 345 fibers (Table 1) with a more pronounced pore directionality (Table 2). The increased length of FN fibers
 346 is consistent with the elongated phenotype of the TGF- β 1-treated fibroblasts that assemble them. The
 347 statistically significant increase in pore directionality of tumor-like matrices compared to normal FN
 348 matrices is in agreement with published reports⁽²⁶⁾ of higher FN alignment in cell-derived matrices
 349 from cancer-associated fibroblasts and in tumor tissue. Detailed results, including the average area and
 350 number of identified anomalous clusters, at multiple thresholds, for four FN variants, are presented in
 351 Supplementary TableS1-TableS8.

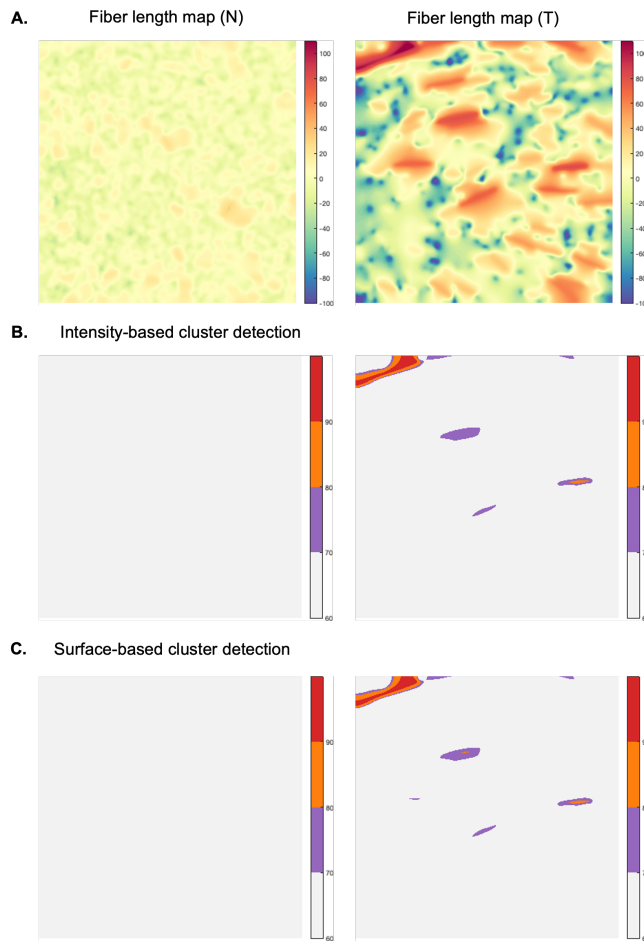


Figure 7. Qualitative analysis - Anomalous cluster detection (with respect to the normal statistical model), applied to two samples of fiber length map (FN B-A+ tumor-like), 1024x1024 pixels, 0.27 $\mu\text{m}/\text{pixel}$ (A), (B) and (C) depict the anomalous clusters ($p\text{val} \leq 0.05$) at various intensity thresholds (70,80,90).

Table 1. Quantitative analysis for detection of differences in fiber length - Anomalous cluster quantification (with respect to the normal statistical model, at $p\text{val} \leq 0.05$), for the comparison of normal (N) and tumor-like (T) FN (1024x1024 pixels, or 276.48 $\mu\text{m} \times 276.48 \mu\text{m}$). The average number of significant clusters per test database for each variant is shown here, for either surface or intensity criteria, if higher than for the normal model, at any selected threshold. Average number of clusters detected in fiber length maps, for normal vs tumor-mimicking FN, for one of the test thresholds (70,80,90).

FN variant	Average number of clusters for (N) vs (T) FN
B-A-	0.43 (surface)
B+A-	0.88 (intensity); 0.92 (surface)
B-A+	0.72 (intensity); 0.78 (surface)
B+A+	0.94 (intensity); 0.94 (surface)

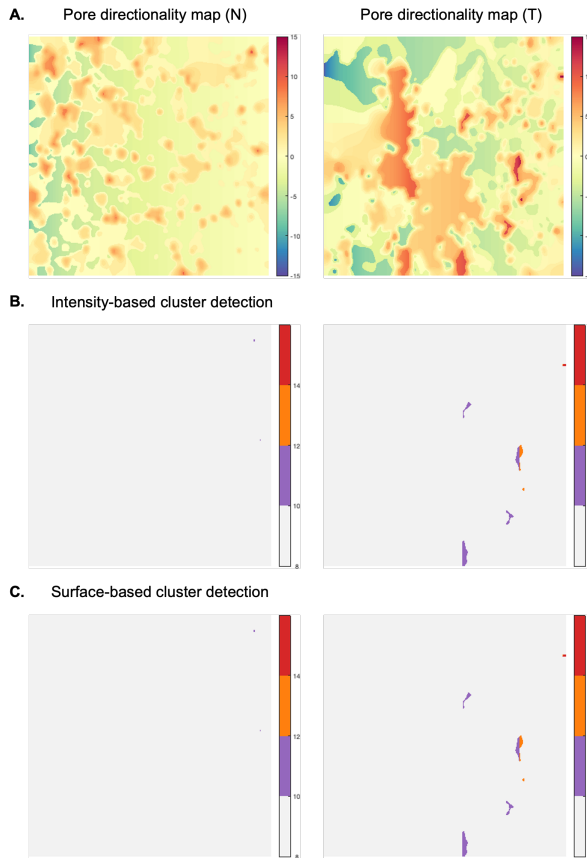


Figure 8. Qualitative analysis - Anomalous cluster detection (with respect to the normal statistical model), applied to two samples of pore directionality map (FN B-A+ tumor-like), 1024x1024 pixels, 0.27 $\mu\text{m}/\text{pixel}$ (A), (B) and (C) depict the detected clusters ($p\text{val} \leq 0.05$) at various intensity thresholds (10,12,14).

Table 2. Quantitative analysis for detection of differences in pore directionality - Anomalous cluster quantification (with respect to the normal statistical model, at $p\text{val} \leq 0.05$), for the comparison of normal (N) and tumor-like (T) FN (1024x 1024 pixels, or 276.48 μm x 276.48 μm). The average number of significant clusters per test database for each variant is shown here, for either surface or intensity criteria, if higher than for the normal model, at any selected threshold). Average number of clusters detected in pore directionality maps, for normal vs tumor-mimicking FN, for one of the test thresholds (10,12,14). '-' is recorded if no significant detection was present.

FN variant	Average number of clusters for (N) vs (T) FN
B-A-	0.12 (intensity)
B+A-	0.22 (surface)
B-A+	0.14 (intensity); 0.34 (surface)
B+A+	-

352 6. Discussion and conclusion

353 The proposed methodology was designed to quantify the differences in terms of spatial organization
 354 between normal and disease-like architectures of variant-specific FN matrices generated *in vitro*. We

355 have previously been able to discriminate the matrix patterns of four alternatively spliced FN variants
356 deposited by cultured fibroblasts using different learning approaches and relying on graph-based feature
357 analysis. The pipeline which includes steps for fiber detection and representation⁽¹¹⁾, and generation
358 of parametric fiber maps is available with a MATLAB GUI: both graph and Gabor filter-based fiber
359 features can be extracted from different images representing fiber networks (e.g. ECM-specific proteins)
360 for downstream analysis. In principle, the steps required for the characterization of ECM (i.e. fiber
361 detection and representation using graphs) in cell-derived matrices generated by cells of different origin
362 remain the same. However, in the case of tissue samples, the ECM is more complex and heterogeneous,
363 and further pre-processing steps may be needed to filter structures that are normally found in tissues
364 (e.g. blood vessels). The number and type of additional steps, however, is dependent on the type of
365 organ/tissue, the pathology under evaluation, and the staining procedure.

366 Here, we developed a statistical parametric map framework for the quantitative and qualitative anal-
367 ysis of fibers, capable of simultaneously detecting and measuring variations of specific ECM features
368 within two different tissue conditions. Importantly, our approach can be evaluated on parametric maps
369 at different thresholds, producing results that are more reliable and statistically relevant (by providing
370 a pval) than a simple hard thresholding of the parametric maps. Our framework was tested using two
371 relevant fiber features, fiber length and pore directionality, whose parametric maps revealed significant
372 differences between normal and disease-mimicking states. However, parametric maps can be extended
373 to include other fiber or pore-specific parameters (e.g. fiber density, width, length, orientation, wavi-
374 ness, and straightness), which could be useful for differentiating among various biological networks in
375 normal and pathological states.

376 Computational analyses of ECM structures can provide essential information about their role in
377 shaping the cellular microenvironment topology in health and during disease progression. Prognostic
378 ECM-specific signatures have already been inferred in cancer-related studies, and in diseases with
379 prominent fibrosis^(27–29). There is also a growing interest in the integration of cell and ECM analyses
380 in a spatially resolved manner to further understand the interactions between cells and their matrix
381 microenvironment⁽³⁰⁾. Indeed, the present work proposing a versatile pipeline for the analysis of ECM
382 produced by cultured fibroblasts, is being extended to studies of ECM organization in human tumor
383 tissue and aims to integrate the phenotypes of cellular components. Hence, a combined local analysis
384 of parametric maps and metrics describing the organization/morphology of adjacent cells (e.g. tumor,
385 immune, vascular cells) will potentially help elucidate the complex interplay between cellular and non-
386 cellular components of the tumor microenvironment.

387 **7. Materials and methods**

388 **7.1. Materials and FN preparations**

389 Recombinant human TGF- β 1 was from R&D Systems Inc. (Minneapolis, MN, USA). All other chem-
390 icals and reagents were purchased from Sigma Aldrich (St Louis, MO, USA) unless otherwise stated.
391 Purified recombinant FN variants were produced as previously described⁽¹¹⁾.

392 **7.2. Cells and culture conditions**

393 *Fnl* $-/-$ mouse kidney fibroblasts were generated and cultured as previously described⁽¹¹⁾. For exper-
394 iments, FN was depleted from fetal calf serum using gelatin sepharose-4B columns (GE Healthcare,
395 Uppsala, Sweden), and the culture medium was supplemented with Penicillin-Streptomycin 100 U/ml
396 and, where indicated, TGF- β 1 (5 ng/ml). Absence of Mycoplasma sp. contamination was routinely
397 verified by PCR as described elsewhere⁽³¹⁾.

7.3. Generation of fibroblast-derived matrices, immunofluorescence staining and microscopy

Fibroblast-derived matrices were generated as described previously. For FN immunostaining, primary antibody (rabbit polyclonal anti-FN) was from Merck-Millipore (Darmstadt, Germany). Fluorescently-labeled (Alexa Fluor 488-conjugated) secondary antibody was from Thermo Fisher Scientific (Waltham, Massachusetts). After staining, the coverslips were mounted in ProLong® Gold antifade reagent (Thermo Fischer Scientific). Confocal imaging was performed on a Zeiss LSM710 confocal system equipped with a 10X/0.45 NA objective. For visual representation, image treatment was performed using Fiji⁽³²⁾.

Acknowledgements. We thank the members of the Adhesion Signaling and Stromal Reprogramming in the Tumor Microenvironment team for critical discussion on the manuscript, iBV PRISM imaging platform for the use of their machines and support, in particular, Sébastien Schaub.

Funding Statement. This work was supported by the French Government (National Research Agency, ANR) through the 'Investments for the Future' LABEX SIGNALIFE: program reference ANR-11- LABX-0028-01, ANR-16-CE93-0005 (ANGIO-FIB), ANR-19-P31A-0002 (31A Côte d'Azur) and La Fondation ARC (PJA20151203207).

Competing Interests. The authors declare no competing interest.

Data Availability Statement. Sample image data and code can be found on the GitHub platform: github.com/aigrapa/ECM-fiber-graph.

Ethical Standards. The research meets all ethical guidelines, including adherence to the legal requirements of the study country.

Author Contributions. Conceptualization: A-I.G;G.E;L.B-F;E.V.O-S;X.D. Methodology: A-I.G;G.E;L.B-F;E.V.O-S;X.D. Data curation: A-I.G;G.E;L.B-F;E.V.O-S;X.D. Data visualisation: A-I.G;G.E;L.B-F;E.V.O-S;X.D. Funding acquisition, Supervision, Writing-review and editing:L.B-F;E.V.O-S;X.D. Writing original draft: A-I.G;G.E. All authors approved the final submitted draft.

Supplementary Material. A supplementary file has been provided for submission.

References

- Poline JB, Worsley KJ, Evans AC & Friston KJ (1997) Combining Spatial Extent and Peak Intensity to Test for Activations in Functional Imaging. *NeuroImage*.Feb;**5**(2):83–96.
- Friston K, Worsley K, Frackowiak R, Mazziotta J & Evans A (1994) Assessing the Significance of Focal Activations Using Their Spatial Extent. Vol. 1, *Human Brain Mapping* 210–20.
- Frantz C, Stewart KM & Weaver VM (2010) The extracellular matrix at a glance. *Journal of Cell Science* Dec 15;**123**(24):4195–200.
- Afratis NA & Sagi I (2019) Novel Approaches for Extracellular Matrix Targeting in Disease Treatment. *The Extracellular Matrix*, New York, NY: Springer New York; p. 261–75.
- Nia HT, Munn LL & Jain RK (2020) Physical traits of cancer *Science*, Oct 30;**370**(6516):eaaz0868.
- Conklin MW, Eickhoff JC, Riching KM, Pehlke CA, Eliceiri KW, Provenzano PP, et al (2011) Aligned collagen is a prognostic signature for survival in human breast carcinoma *American Journal of Pathology* ;**178**(3):1221–32.
- Provenzano PP, Eliceiri KW, Campbell JM, Inman DR, White JG & Keely PJ (2006) Collagen reorganization at the tumor-stromal interface facilitates local invasion. *BMC Med* Dec;**4**(1):38.
- Burke K, Smid M, Dawes RP, Timmermans MA, Salzman P, van Deurzen CHM, et al. (2015) Using second harmonic generation to predict patient outcome in solid tumors *BMC Cancer* Dec;**15**(1):929.
- Hynes RO (2009) The extracellular matrix: Not just pretty fibrils *Science* Nov 27;**326**(5957):1216–9.
- Barker TH & Engler AJ (2017) The provisional matrix: setting the stage for tissue repair outcomes. *Matrix Biology* Jul;**60–61**:1–4.
- Efthymiou G, Radwanska A, Grapa A-I, Beghelli-de la Forest Divonne S, Grall D, Schaub S, et al (2021) Fibronectin Extra Domains tune cellular responses and confer topographically distinct features to fibril networks *Journal of Cell Science* Feb 24;**134**(jcs252957).
- Efthymiou G, Saint A, Ruff M, Rekad Z, Ciais D & Van Obberghen-Schilling E (2020) Shaping Up the Tumor Microenvironment With Cellular Fibronectin. *Front Oncol*. Apr 30;**10**:641.
- Adler RJ (2010) The Geometry of Random Fields. *Society for Industrial and Applied Mathematics*. Available from <http://epubs.siam.org/doi/book/10.1137/1.9780898718980>.

- 447 14. Worsley K.J., Evans A.C., Marrett S., & Neelin P., (1992) A Three-Dimensional Statistical Analysis for CBF Activation
 448 Studies in Human Brain, *Journal of Cerebral Blood Flow & Metabolism*, **12**(6):900-918, [10.1038/jcbfm.1992.127](https://doi.org/10.1038/jcbfm.1992.127).
- 449 15. Lafarge F, Descombes X & Zerubia J (2004) Détection de feux de forêt par analyse statistique de la radiométrie d'images
 450 satellitaires HAL. Available from <https://hal.inria.fr/inria-00070634>.
- 451 16. Peyré G & Cuturi M (2019) Computational Optimal Transport: With Applications to Data Science (2019), *Foundations and
 452 Trends® in Machine Learning*, 1935-8237 vol **11**, 5-6, 355-607.
- 453 17. Peyré G (2011) The Numerical Tours of Signal Processing - Advanced Computational Signal and Image Processing *IEEE
 454 Computing in Science and Engineering* Available from <https://hal.archives-ouvertes.fr/hal-00519521/document>.
- 455 18. Morrill EE, Tulepbergenov AN, Stender CJ, Lamichhane R, Brown RJ & Lujan TJ (2016) A validated software application
 456 to measure fiber organization in soft tissue *Biomech Model Mechanobiol* Dec; **15**(6):1467–78
- 457 19. Wershof E, Park D, Barry DJ, Jenkins RP, Rullan A, Wilkins A, et al (2021) A FIJI macro for quantifying pattern in
 458 extracellular matrix *Life Sci Alliance* Mar; **4**(3):e202000880
- 459 20. Liu Y, Keikhosravi A, Pehlke CA, Bredfeldt JS, Dutton M, Liu H, Mehta GS, Claus R, Patel AJ, Conklin MW, Inman DR,
 460 Provenzano PP, Sifakis E, Patel JM, Eliceiri KW (2020) Fibrillar Collagen Quantification With Curvelet Transform Based
 461 Computational Methods. *Front Bioeng Biotechnol*. Apr 21; **8**:198.
- 462 21. Grapa A-I (2020) Characterization of fibronectin networks using graph-based representations of the fibers from 2D confocal
 463 images. *PhD thesis, Université Côte d'Azur*, 2020COAZ4031. Available from <https://theses.hal.science/tel-03052167/file/2020AZUR4031.pdf>
- 464 22. Kollmannsberger P, Kerschnitzki M, Repp F, Wagermaier W, Weinkamer R, & Fratzl P (2017) The small world of
 465 osteocytes: Connectomics of the lacuno-canalicular network in bone *New Journal of Physics* Jul 1; **19**(7).
- 466 23. Aguilar W, Martínez-Pérez ME, Frauel Y, Escolano F, Lozano MA, & Espinosa-Romero A (2007) Graph-Based Methods
 467 for Retinal Mosaicing and Vascular Characterization. *Graph-Based Representations in Pattern Recognition, Lecture Notes
 468 in Computer Science* Springer Berlin Heidelberg; vol. **4538** p. 25–36.
- 469 24. Bresenham JE (1998) Algorithm for computer control of a digital plotter. *Seminal graphics*, ACM New York, NY, USA: p.
 470 1–6. Available from <https://dl.acm.org/doi/10.1145/280811.280913>
- 471 25. D'Errico J (2021) Interpolation and extrapolation of elements in a 2D array [Internet]. *MATLAB Central File Exchange*.
 472 Retrieved October 12, 2021.; Available from <https://www.mathworks.com/matlabcentral/fileexchange/4551-inpaintnans>
- 473 26. Park D., Wershof E., Boeing S, et al. (2020) Extracellular matrix anisotropy is determined by TFAP2C-dependent regulation
 474 of cell collisions *Nat. Mater.* **19**, 227–238.
- 475 27. Parker A.L., Bowman E., Zingone A. et al. (2022) Extracellular matrix profiles determine risk and prognosis of the
 476 squamous cell carcinoma subtype of non-small cell lung carcinoma *Genome Med* **14**, 126.
- 477 28. Feng D., Ngov C., Henley N. et al. (2019) Characterization of Matricellular Protein Expression Signatures in Mechanisti-
 478 cally Diverse Mouse Models of Kidney Injury. *Sci Rep* **9**, 16736.
- 479 29. Merl-Pham J, Basak T, Knüppel L, Ramanujam D, Athanason M, Behr J, Engelhardt S, Eickelberg O, Hauck SM,
 480 Vanacore R, Staab-Weijnitz CA. (2019) Quantitative proteomic profiling of extracellular matrix and site-specific collagen
 481 post-translational modifications in an in vitro model of lung fibrosis *Matrix Biol Plus*. Apr 13; **1**:100005.
- 482 30. Vasiukov G, Novitskaya T, Senosain MF, Camai A, Menshikh A, Massion P, et al (2021) Integrated Cells and Collagen
 483 Fibers Spatial Image Analysis *Front Bioinform*. Nov 8; **1**:758775.
- 484 31. Kong F, James G, Gordon S, Zelynski A & Gilbert GL (2001) Species-Specific PCR for Identification of Common
 485 Contaminant Mollicutes in Cell Culture. *Appl Environ Microbiol*. Jul; **67**(7):3195–200.
- 486 32. Schindelin J, Arganda-Carreras I, Frise E, Kaynig V, Longair M, Pietzsch T, et al (2012) Fiji: an open-source platform for
 487 biological-image analysis *Nat Methods*. Jul; **9**(7):676–82.